REVIEW

Modeling the structure and thermodynamics of high-entropy alloys

Michael Widom[a)]
Department of Physics, Carnegie Mellon University, Pittsburgh, Pennsylvania 15213, USA

High-entropy and multiprincipal element alloys present exciting opportunities and challenges for computational modeling of their structure and phase stability. Recent interest has catalyzed rapid development of techniques and equally rapid growth of new results. This review surveys the essential concepts of thermodynamics, total energy calculation, and the bridge between them provided by statistical mechanics. Specifically, we review the electronic density functional theory of alloy total energy as applied to supercells and special quasirandom structures. We contrast these with the coherent potential approximation and semi-empirical approximations. Statistical mechanical approaches include cluster expansions, hybrid Monte Carlo/molecular dynamics simulations, and extraction of entropy from correlation functions. We also compare first-principles approaches with Calculation of Phase Diagrams and highlight the need to augment experimental databases with first-principles derived data. Numerous example applications are given highlighting recent progress utilizing the concepts and methods that are introduced.

I. INTRODUCTION

Modeling the structure and the thermodynamics of multicomponent materials presents a number of interesting and exciting scientific challenges. Recently developed multicomponent alloy systems stand in contrast to traditional alloys, which traditionally contain just one or two primary constituent chemical species, with other species present in small concentrations. Current research pays increasing attention to multiprincipal element alloy[1,2] (MPEA) systems containing many chemical species. Special effort is given to complex concentrated alloys,[3] in which several elements are present simultaneously in high concentrations. Cases where the elements substitute freely are known as concentrated solid solution alloys[4] (CSSAs), while the specific case where multiple elements are present in high concentration, and they also substitute freely, are termed high-entropy alloys[2] (HEAs). This review focuses on CSSAs and HEAs.

Stabilization of a single phase through entropy of mixing is a foundational notion of HEAs. The ideal configurational entropy of chemical substitution,

$$S_{\text{chem}} = -k_{\text{B}} \sum_{\alpha} x_{\alpha} \ln x_{\alpha} \quad , \qquad (1)$$

is maximized when all elements substitute freely, which inhibits separation into multiple phases. It is also

maximized when all lattice sites are equivalent, which tends to favor simple crystal Bravais lattice structures such as face-centered cubic (FCC) and body-centered cubic (BCC) whose primitive cells contain only a single site, or hexagonal close packed (HCP) whose primitive cell contains two equivalent sites. Finally, it is maximized as a function of composition x_{α} when all species are present in equal proportions, i.e., $x_{\alpha} = 1/N$ for N species. In this case, $S_{\text{chem}} = k_{\text{B}} \ln N$. The greater the number of species, the greater the value of Schem, hence motivating the search for equiatomic or nearly equiatomic compounds with large N.

Despite the increase of S_{chem} for a random solid solution with increasing N, thermodynamic stability depends on minimizing the Gibbs free energy,

$$G(N, P, T; \mathbf{x}) = H - TS \quad , \qquad (2)$$

with H the enthalpy. As the number of constituents grows, the range of pairwise chemical interaction strengths tends to grow. It may turn out that associating groups of strongly interacting chemical species to reduce H minimizes the free energy more effectively than maximizing the entropy does, leading to phase separation. Thus taking N large may be a counterproductive strategy for seeking thermodynamic stability.[5] Owing to the factor of absolute temperature T multiplying the entropy S, enthalpy always wins out at low temperature. A second effect further diminishes the advantage of taking N large; as the number of species grows, so too does the number of potential competing phases, further reducing the chances of stabilizing a single phase.[6]

[a)]Address all correspondence to this author.
e-mail: widom@cmu.edu

AU1

As seen from Eq. (2), to predict the stability of a given alloy system requires calculating both the enthalpy (i.e., the energy at fixed pressure) and the entropy. Accurate calculation of the enthalpy depends on precise understanding of interatomic interactions. While this can be achieved in particular cases using empirical potentials, fitting such potentials becomes increasingly difficult as the number of species grows. Hence a parameter-free first-principles approach is advantageous, and this will be the primary focus of this review. The entropy, also, presents significant challenges. First of all, the total entropy has many contributions,

$$S = S_{vib} + S_{chem} + S_{elec} + S_{mag} + \cdots \quad , \qquad (3)$$

where each term represents a different physical process and must either be calculated or its neglect must be justified. Expression (1) for S_{chem} is itself only a simplified approximation, based on the assumption of a totally random distribution. In reality, chemical interactions correlate the occupation probabilities of different chemical species on nearby lattice sites. These correlations reduce S_{chem} below the ideal value.

In the following, we first review the basic thermodynamic laws that govern phase stability and phase diagrams. Then, we turn to methods to calculate the energy and enthalpy. Here, our main focus is on the quantum mechanics-based first-principles total energy calculation within the approximation of electronic density functional theory (DFT). However, we do address the use of fitted interaction potentials and also the empirical Miedema energy model. Given an energy calculation method, we still need to provide a structure model to which it will be applied. For disordered solid solutions, we will discuss the coherent potential approximation (CPA), and supercell methods including special quasirandom structures (SQS[7]).

Methods of statistical mechanics are required to incorporate entropy into the free energy. We will discuss each contribution to Eq. (3) separately and explain in detail how it may be calculated. Then, we will concentrate on the problem of S_{chem} and how to account for nonideal mixing. Here, we will describe the use of cluster expansion approximations to total energy and an alternative method based on direct simulation through a hybrid application of Monte Carlo and molecular dynamics. We discuss, as an aside, the revisions needed in the event of sublattice ordering.

Calculation of Phase Diagrams (CALPHAD[8]) provides an alternative approach to thermodynamic prediction. Based on the interpolation of empirical thermodynamic functions fitted to existing experimental or first principles-derived data, it is a powerful tool for phase diagram prediction. However, its applicability to HEAs and more general CSSAs depends on the availability of thermodynamic databases that are often incomplete, or the combination of existing databases that are mutually inconsistent. We survey the existing databases for HEAs and address the strategy for augmenting them with first-principles-derived data.

Finally, we give concrete examples of these methods in action, taken from the existing literature. Specifically, we examine applications of the CPA, supercells, database mining, and cluster expansions. Owing to the great interest in HEAs and related compounds, many other books[9,10] and review articles[3,11–16] exist that cover similar topics to this one. This interest is motivated both by their intrinsic fundamental scientific interest and also by their potential applications that exploit their promising mechanical[17–20] and other properties.[21–27]

II. THERMODYNAMICS

The centerpiece of alloy thermodynamics is the Gibbs free energy, $G(N, P, T; \mathbf{x})$, which depends on the total number of atoms N, the pressure P, and the temperature T. When more than a single chemical species is present, we must specify the number of atoms of each type, $N_\alpha = x_\alpha N$, hence defining the mole fractions x_α subject to the constraint $\sum x_\alpha = 1$. We collect the full set of mole fractions $\{x_\alpha\}$ into a single vector $\mathbf{x}$. The space of compositions $\mathbf{x}$ is a simplex in $N - 1$ dimensions: the single point $\mathbf{x} = 1$ for $N = 1$ the line $0 \leq x \leq 1$ for $N = 2$, a triangle for $N = 3$, etc. As expressed previously in Eq. (2), G can be separated into the enthalpy $H = E + PV$, with E the energy and V the volume, and an entropic contribution $-TS$, with S the entropy. For solid materials at atmospheric pressure, the product PV is generally negligible and we may consider the enthalpy as simply the energy of the structure under the condition $P = 0$. G has a special numerical value related to the chemical potentials μ_α,

$$G = \sum_\alpha \mu_\alpha N_\alpha \quad . \qquad (4)$$

Under certain circumstances, multiple phases i may be present, each containing the number of atoms $N^{(i)}$ at composition $\mathbf{x}^{(i)}$, resulting in free energy $G(N, P, T; \mathbf{x}) = \sum_i G^{(i)}$ with $G^{(i)}(N^{(i)}, P, T; \mathbf{x}^{(i)}) = \sum_\alpha \mu_\alpha x_\alpha^{(i)} N^{(i)}$.

In thermal equilibrium, the pressure P, the temperature T, and the individual chemical potentials μ_α are shared in common among all phases because the equilibrium state minimizes the total free energy, G. Indeed, the total free energy G is obtained as the convex hull of the set of all functions $G^{(i)}(N^{(i)}, P, T; \mathbf{x}^{(i)})$ defined over the composition space. Within a single phase, $G^{(i)}$ varies smoothly, and the slope with respect to composition variables $x_\alpha^{(i)}$ yields

the chemical potential μ_α. When phases coexist, G varies linearly along the tie-line or tie-plane of common tangency. If all phases had definite stoichiometry, i.e., they exist only at unique compositions $\mathbf{x}^{(i)}$, the convex hull G may be easily obtained through the optimization method known as linear programming; the more general case of continuously varying $G^{(i)}$ becomes a nonlinear optimization problem that is more difficult to solve.

From the differential

$$dG = VdP - SdT + \sum_\alpha \mu_\alpha dN_\alpha \quad , \qquad (5)$$

we see there are $N + 2$ free variables. If the system has p phases in equilibrium, p independent Gibbs–Duhem relations of the form

$$\sum_\alpha N_\alpha^{(i)} d\mu_\alpha = VdP - SdT \quad , \qquad (6)$$

must be obeyed. Hence $F = N + 2 - p$ thermodynamic degrees of freedom may be varied while remaining under the condition of phase coexistence. Equivalently at most $N + 2$ phases may coexist in equilibrium. However, metallurgical experiments are frequently performed at atmospheric pressure, removing one degree of freedom. Hence at any particular chosen temperature (thus removing a second degree of freedom), at most N phases may coexist. At an arbitrarily chosen composition $\mathbf{x}$, concentrated intermetallic systems typically exhibit the maximum number of possible coexisting phases. It is quite rare for an equiatomic multicomponent alloy to exist as a single phase in equilibrium.

When elements combine to form a compound, we define the changes, ΔG, ΔH, and ΔS, as the free energy, enthalpy, and entropy of formation. For example, the free energy of formation is the free energy of the compound minus the composition-weighted average of the pure element free energies. Negative free energy of formation means that it is thermodynamically favorable for the elements to combine and form the compound. Since ΔG differs from G by a linear function of composition, they share the same set of states on their convex hulls, namely the set of thermodynamically stable states.

III. FIRST-PRINCIPLES TOTAL ENERGY

A. DFT

The total energy of a crystal structure is a function of atomic positions and their chemical species. While an explicit form for that function is not known exactly, a variety of computational methods exist to approximate it that we survey here. A suitable starting point, and the most accurate method that is practical to apply, is known as electronic DFT[28]. This approach treats the atomic

positions as classical variables, describing the structure through a set of positions $\{\boldsymbol{R}_i\}$ and their atomic numbers Z_i. The electrons, in contrast, are treated quantum mechanically, capturing the nature of interatomic bonding and its variation with respect to the individual chemical nature of different atomic species. That is, we apply the Born–Oppenheimer approximation to separate classical (atomic) degrees of freedom from quantum (electronic).

In principle, the electrons are described by a many-body wavefunction obeying antisymmetry under exchange of electron pairs. Each electron is subject to a potential energy of interaction with every other electron and also with every ionic core. In practice that problem cannot be solved for more than a small number of electrons. Instead we replace the exact many-body Schrodinger equation with a set of approximate single-electron Schrodinger equations known as the Kohn–Sham equations.[29]

$$\left(-\frac{\hbar^2}{2m} \nabla^2 + V_{\text{eff}}(\boldsymbol{r}) \right) \psi_i = E_i \psi_i \quad . \qquad (7)$$

Here, each electron is subject to an effective potential V_{eff} that includes the Coulomb interaction with the ionic cores, a Hartree potential due to the interaction with the average density of all electrons, and an additional term known as the exchange-correlation potential $V_{\text{XC}}[\rho(\boldsymbol{r})]$ that is a functional of the global electron density $\rho(\boldsymbol{r})$, whose form must be approximated. Popular choices for V_{XC} include the local density approximation,[30] in which the potential at position $\boldsymbol{r}$ depends only on the values of the electron density ρ at that point, and the generalized gradient approximation,[31] in which the potential at $\boldsymbol{r}$ depends both on the value of ρ and on its gradient.

Because V_{eff} depends on the electron density $\rho(\boldsymbol{r}) = \sum_i |\psi_i(\boldsymbol{r})|^2$, with the sum over all occupied electron states, the equations must be solved self-consistently. Even within the density functional approximation, solutions can be difficult owing to rapid variation of ψ_i near the ionic cores. A further approximation based on pseudopotentials or the projector augmented wave method[32,33] alleviates this difficulty by special treatment of the core region and treating only outer shell valence electrons.

A number of computer programs that are widely available or even public domain solve the Kohn–Sham equations to yield total energies that can be accurate to within a few meV/atom (a few tenths of a Joule/mole). This is sufficient in most cases to identify favorable low energy structures of alloys, with the convex hull of enthalpy versus composition reproducing the experimentally known low temperature stable phases.[34,35] A wealth of additional information comes as a side benefit, including the electronic wavefunctions and density of states $D(E)$, which

J. Mater. Res., Vol. 0, No. 0, 2018

3

govern the electrical conductivity, optical spectra, and the electronic free energy F_{elec}; the ground state charge density $\rho(\boldsymbol{r})$, which reveals the nature of chemical bonding; forces acting on individual atoms, which can be used to relax the atoms to their stable positions, to calculate phonon vibrational density of states $g(\omega)$, or to perform ab initio molecular dynamics[36]; the mechanical stress tensor of the complete structure, which can be used to optimize the volume and to calculate elastic constants.

B. Supercell and SQS

Since DFT calculation requires the positions and chemical identities of every atom as input, special consideration is required to calculate the entropy of a random solid solution. We can exploit the large volume and large number of atoms in bulk matter to address this problem through averaging in the thermodynamic limit. Think of the bulk system as consisting of many over-lapping subregions; we could calculate the energy of many such subregions (invoking the "nearsightedness" of the electronic structure[37]), then approximate the bulk as an average over local regions, weighted by their fre-quency in the bulk.

Bravais lattice structures such as FCC and BCC contain only a single atom in their primitive cell, which is then repeated infinitely to fill space. To explicitly form a structure of N chemical species requires at least N atoms (and even more if their concentrations x_α are not equal), hence motivating the concept of a supercell containing several contiguous primitive cells, that itself can be repeated infinitely to fill space. The chemically decorated supercell is thus a unit cell of a more complex non-Bravais lattice structure. Given a supercell of S atomic sites, and N_1, N_2, ..., N_s atoms of species 1, 2, ..., s to occupy them, the number of possible decorations of the supercell, $S!/N_1!N_2!...N_s!$ grows very rapidly with the size S of the supercell. Fortunately, owing to the law of large numbers, sampling a subset of possible supercell decorations is sufficient to obtain an excellent average.

An alternative to sampling many decorations of a supercell is to design a special structure that represents a typical decoration. In a maximally random (uncorre-lated) solid solution, the probability for a given inter-atomic bond to connect species α and β is $y_{\alpha\beta} = x_\alpha x_\beta$, similarly any triplet has probability $w_{\alpha\beta\gamma} = x_\alpha x_\beta x_\gamma$ and any quadruplet has probability $z_{\alpha\beta\gamma\delta} = x_\alpha x_\beta x_\gamma x_\delta$. How-ever, in a supercell of modest size (see Fig. 1) there can be large deviations from these frequencies. SQS[7] are specially designed to match selected correlation func-tions, typically including the first few neighbor pairwise bonds but rarely including a triplet or a quadruplet. There is a danger that optimizing certain correlation functions may strongly skew others, resulting in a highly un-representative structure. An example of the unreliability

of SQS is provided in Fig. 2, which shows the variation in energy with respect to differing assignments of chemical species to the 4 site classes in a 4-component 64-atom equiatomic SQS.[38] Since there are 24 ways to assign 4 species to 4 site classes, there are a total of 24 inequivalent configurations. If the SQS were truly repre-sentative, the energy should not depend on which element is assigned to a given site class.

Sensitivity to chemical species distribution should diminish with increasing supercell size S, and these can be efficiently generated through Monte Carlo methods.[39] The supercell should be chosen large enough to allow variation of local environments, but not so large that the $O(S^3)$ scaling of DFT calculation time renders the calculations prohibitively expensive. If phonon calcula-tions are to be performed, the calculation time grows as $O(S^4)$ because of the requirement to displace each atom independently. An alternative to the SQS approach is to sample a variety of specific ordered structures utilizing the "small set of ordered structures" approach.[40]

C. CPA

The CPA[41] sidesteps the need to explicitly assign chemical species to sites. The electronic structure problem is solved by a Green function method based on the multiple scattering of electrons off atomic potentials. Each atom of species α is assumed to be surrounded by effective atoms placed on the remaining lattice sites, whose scattering potential is given by the composition-weighted average of all atomic species. The set of species-dependent scattering potentials is then solved self-consistently. Every atom feels an identical environment, avoiding the arbitrar-iness implicit in supercell methods. Furthermore, the composition can be varied continuously. However, there are disadvantages as well. First, the effective atom is a fiction, and the resulting uniformity of environment is not correct. Second, because all surrounding lattice sites are identically occupied, each atom sits in a position of high symmetry and experiences no force displacing it from its own lattice site so that lattice distortion is absent.

D. FP-tuned pair potentials and EAM

Because of the computational requirements of DFT, it can be useful to trade chemical accuracy for speed and simplicity through the use of empirical potentials. The simplest of these are pair potentials, in which atoms interact pairwise, resulting in a simple expression for the total potential energy

$$V = \sum_{\alpha \leq \beta} \sum_{i < j} V_{\alpha\beta}(r_{ij}) \quad , \qquad (8)$$

where the pair potential $V_{\alpha\beta}(r_{ij})$ is the interaction of the ith atom of species α with the jth atom of species β. The
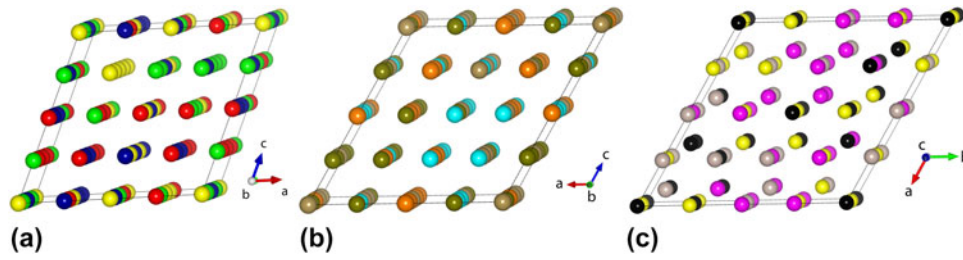
FIG. 1. Four-component SQS structures for (a) FCC, (b) BCC, and (c) HCP alloys (reprinted with permission from Ref. 38). Each color represents a different SQS site class. (color online)
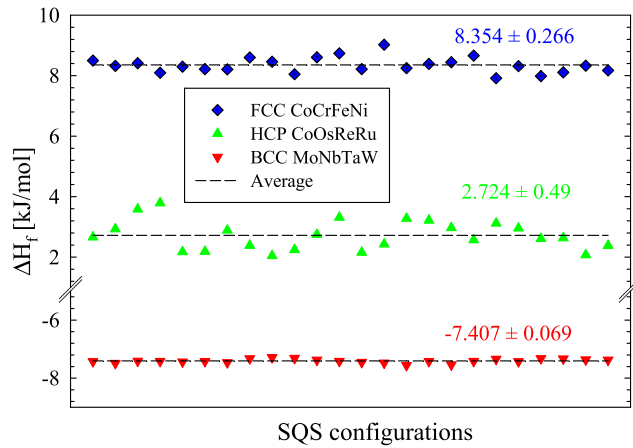

FIG. 2. Energy variation for different assignments of elements to SQS site classes (reprinted with permission from Ref. 38). CoCrFeNi is FCC, CoOsReRu is HCP, and MoNbTaW is BCC, and the SQS structures are illustrated in Fig. 1. (color online)

inequalities ensure that each bond is counted exactly once. The pair potential can be defined in terms of simple functions such as Lennard-Jones ("6–12"), Morse, Johnson, or they can be derived from perturbation theory.[42–44] The Friedel oscillations caused by insertion of metal ions into the electron gas can often be captured using a simple oscillatory function.[45] One peculiarity of pair potentials is that they exert only central forces, and hence the Cauchy relation among elastic constants (e.g., $C_{12} = C_{44}$ for centrosymmetric cubic crystals) is automatically obeyed. The Cauchy relation does not hold in real materials.

An important generalization of the pair potential adds a nonlinear function of pairwise functions. The embedded-atom class of interactions[46,47] (this also includes Finnis–Sinclair[48] and Johnson[49] potentials) is defined by

$$V = \sum_{\alpha \leq \beta} \sum_{i < j} V_{\alpha\beta}(r_{ij}) + \sum_{\alpha} \sum_{i} E\left(\sum_{\beta} \sum_{j} \rho_{\alpha\beta}(r_{ij}) \right) \quad .$$

(9)

Here, the "embedding function" E represents a contribution to the energy of atom i of type α embedded in the electron density created by neighboring atoms of type β at distance r_{ij}. Embedded atom potentials exert noncentral many-body forces and thus are able to violate the Cauchy violate (i.e., exhibit proper elastic behavior). They also capture certain surface reconstructions such as contracted bond lengths near metallic surfaces.[46]

Pair potentials and embedded atom-type potentials based on analytic functions contain parameters that must be defined separately for each pair of species $\alpha\beta$. These parameters can be fit to reproduce properties such as lattice constants (atomic size) and binding strength or elastic constants. In practice, the number of parameters is too low to allow fitting of all physical quantities that may be of interest, resulting in potentials that are satisfactory for certain applications but must be used with caution outside of purposes for which they were designed. Even potentials created in tabulated form or though splines,[50,51] which are far more general than simple analytic functions, will not accurately reproduce properties for which they were not specifically designed because the particular functional forms (8) and (9) are too restrictive and unable to capture the full range of many-body interactions.

Equations (8) and (9) can be evaluated in a time of order S^2, where S is the size of the system (i.e., number of atoms). Note that this is better scaling than obtained by DFT. For sufficiently large systems, the majority of atom pairs lie outside the range of the interaction $V_{\alpha\beta}(r)$ or the electron density $\rho_{\alpha\beta}(r)$. In this case, the scaling can be reduced to order S^1, provided that a list is obtained of which atoms lie with the interaction ranges of each other. However, the fitting of interaction parameters presents a scaling difficulty. If there are N chemical species, of order N^2 parameters must be fit. If changes in composition or density are made, they must be refit. This contrasts with DFT which requires only order N pseudopotentials (or none at all for all-electron methods). Pseudopotentials are widely available in advance and are highly transferable.

E. Miedema model

Finally, the Miedema model[52] provides the simplest approach to calculation of enthalpy. Based on notions of

atomic volume and solvation energy, and originally intended for application to liquids, it defines pairwise interactions of atomic species without regard to the actual crystal structure, resulting in

$$\Delta H_{\alpha\beta} = f(x_\alpha, x_\beta)\left(x_\alpha \Delta H^{\mathrm{sol}}_{\alpha \text{ in } \beta} + x_\beta \Delta H^{\mathrm{sol}}_{\beta \text{ in } \alpha}\right) \quad , \quad (10)$$

with

$$f(x_\alpha, x_\beta) = x_\alpha x_\beta (1 + \delta x_\alpha x_\beta) \quad , \quad (11)$$

representing the surface contact area of species α and β. Tabulated values of parameters are available for many elements. As applied to solid alloys, the Miedema model formation enthalpy contains two additional terms,[53] H_{elastic} for elastic strain of solid solutions, and H_{struct} that discriminates between FCC, HCP, and BCC structures of transition metals and depends on their valence electron counts. Although Miedema defined the model for binary compounds, proposed generalizations to ternaries and beyond exist.[6,54,55] This has been used to screen large numbers of compounds to predict formation of high-entropy metallic glass[56–58] and to investigate formation rules for multicomponent alloys.[59–61]

IV. COMBINING FIRST-PRINCIPLES TOTAL ENERGY WITH STATISTICAL MECHANICS

Section III addressed methods to calculate the energy of a structure, while thermodynamics combines energy and entropy to form the free energy. Statistical mechanics provides the formal bridge between energy and free energy. Several physical excitations (atomic vibrations, chemical substitution, and electronic and magnetic excitations) contribute to the entropy and can be directly computed based on first-principles total energy calculations. Here, we begin by describing direct methods, then address certain convenient approximations.

$$Q = \frac{1}{h^{3N}N!} \int \mathrm{d}\mathbf{r}\mathrm{d}\mathbf{p}\mathrm{d}s e^{-E/k_\mathrm{B}T} \quad . \quad (12)$$

Here $\mathbf{r}$ and $\mathbf{p}$ represent the set of all positions and momenta and s is a collection of other degrees of freedom should they exist (e.g., electronic or magnetic states). We assume that we can calculate E based on either first-principles DFT or else based on interatomic potentials. Frequently, the energy can be decomposed into a sum of independent terms. For example, we can separate the kinetic energy of the atoms $K = \sum_i |\mathbf{p}_i|^2/2m_i$ from the potential energy $V(\mathbf{r}, s)$ to obtain $Q = Z/\Lambda^{3N}$, with the thermal de Broglie wave length $\Lambda = \sqrt{2\pi\hbar^2/mk_\mathrm{B}T}$, and

$$Z = \int \mathrm{d}\mathbf{r}\mathrm{d}s e^{-V(\mathbf{r},s)/k_\mathrm{B}T} \quad . \quad (13)$$

Notice that we assume here a fixed volume V, so the free energy is a Helmholtz free energy $F(NVT)$. We will later discuss the transformation to the Gibbs free energy $G(NPT)$.

For crystalline solids, configuration space separates into basins that relax to distinct structures, and we can label the basin by its relaxed structure Γ. For example, Γ might specify a particular arrangement of chemical species in a random solid solution. Within a basin at sufficiently low temperatures, the system executes small oscillations around Γ. We define a vibrational free energy $F_{\mathrm{vib}}(\Gamma)$ by integrating $e^{-V/k_\mathrm{B}T}$ over the basin containing Γ. Assuming that the small vibrations have little impact on the electronic states, we may also define an electronic free energy $F_{\mathrm{elec}}(\Gamma)$ from the occupation probabilities of single electron states, $f_{T,\mu}(E) = 1/\left(e^{-(E-\mu)/k_\mathrm{B}T} + 1\right)$. In this case, the electronic free energy $F_{\mathrm{elec}}(\Gamma) = U_{\mathrm{elec}} - TS_{\mathrm{elec}}$ with

$$U = \int \mathrm{d}E E D(E)\left(f_{T,\mu}(E) - f_{0,E_\mathrm{F}}(E)\right) \quad , \quad (14)$$

and

$$S = -k_\mathrm{B} \int \mathrm{d}E D(E)\left[f_{T,\mu}(E) \ln f_{T,\mu}(E) + \left(1 - f_{T,\mu}(E)\right) \ln\left(1 - f_{T,\mu}(E)\right)\right] \quad , \quad (15)$$

A. Direct methods

Statistical mechanics defines the free energy as $F = -k_\mathrm{B}T \ln Q$, with the partition function Q obtained from an integral over all degrees of freedom,

$D(E)$ is the electronic density of states, and the chemical potential μ is determined by

$$N_{\mathrm{electrons}} = \int \mathrm{d}E D(E) f_{T,\mu}(E) \quad . \quad (16)$$

At low temperature, μ approaches the Fermi energy E_F, while at high temperatures it may be necessary to compute it exactly from Eq. (16).

The vibrational free energy can be evaluated in the harmonic approximation as

$$F_{\text{vib}} = k_B T \int d\omega\, g(\omega) \ln[2 \sinh(\hbar\omega/2k_B T)] \quad , \quad (17)$$

with $g(\omega)$ the vibrational density of states. This F_{vib} incorporates both the positional and momentum degrees of freedom, canceling the $1/\Lambda^{3N}$ factor relating Q to Z. At high temperatures, the quasiharmonic approximation may be applied to account for thermal expansion by calculating the volume-dependence of vibrational frequencies. Including thermal expansion $V(T)$ converts the Helmholtz free energy $F(N, V, T)$ into the Gibbs free energy $G(N, P, T)$.

Since we have separated (approximately) the electronic and vibrational degrees of freedom, we may define a basin free energy

$$F(\Gamma) = V(\Gamma) + F_{\text{elec}}(\Gamma) + F_{\text{vib}}(\Gamma) \quad , \quad (18)$$

with $V(\Gamma)$ the relaxed energy in basin Γ. Then our partition function becomes $Z = \sum_{\Gamma} e^{-F(\Gamma)/k_B T}$. It may be permissible to make a further approximation, taking F_{vib} and F_{elec} independent of Γ. In this case, the full free energy $F = F_{\text{vib}} + F_{\text{elec}} + F_{\text{config}}$ with $F_{\text{config}} = -kT \ln Z_{\text{config}}$ and

$$Z_{\text{config}} = \sum_{\Gamma} e^{-V/k_B T} \quad . \quad (19)$$

The sum runs over distinct configurations of chemical species on lattice sites. If there is only a single relevant structure, for example, a well-ordered crystalline solid, then no summation is needed and the calculation is complete. For a random solid solution, there can be many terms. Within a sufficiently small supercell, it may be possible to explicitly sum over configurations and obtain a reasonable estimate of the free energy.[62–64] However, the number of configurations grows exponentially with the number of sites, so usually some other method will be required to explore the thermodynamics.

An especially simple approximation is to take the enthalpy, and vibrational and electronic free energies of just a single representative structure (e.g., an SQS), then assign the ideal configurational entropy as in Eq. (1). In the event of chemical ordering onto sublattices[65,66] such as B2 order,[67–69] one sums the sublattice entropies weighted by the fractions of atoms $\{f_i\}$ on each sublattice i,

$$S = -k_B \sum_i f_i \sum_\alpha x_\alpha^{(i)} \ln x_\alpha^{(i)} \quad . \quad (20)$$

More generally, one can apply a mean field theory to represent both the energy and the entropy in terms of unknown short-range order parameters, then determine the order parameters that minimize the free energy.[70] The approximations of Eqs. (1) and (20) are known as the Bragg–Williams approximation.[71] Including pair correlation functions (see below) results in the quasichemical or Bethe approximation,[72,73] while extension to multipoint correlations leads to Kikuchi's cluster variation method.[74,75]

Inclusion of magnetism is also feasible but the magnetic entropy[16] presents difficulties. The magnetic contribution to the enthalpy can be easily obtained through spin-polarized DFT. Many of the popular FCC HEAs based on CoCrFeNi exhibit complex magnetic structure with the Cr atoms tending to order antiferromagnetically relative to the others, leading to the possibility of magnetic frustration. Indeed, multiple self-consistent solutions of the Kohn–Sham equations can be found corresponding to different patterns of positive and negative moments. At low temperatures in the ferromagnetic state, magnetic excitations known as spin waves reduce the magnetization. A rigorous calculation of the magnetic entropy similar to the vibrational entropy can be performed if the spin wave density of states can be calculated. At elevated temperatures in the paramagnetic state, localized moments may persist on the individual atoms but long-range ferromagnetic order is destroyed. In this limit, an effective spin S can be defined for each atom, and the entropy approximated as $k_B \ln(2S + 1)$. Although rigorous calculation of magnetic entropy is not yet available for HEAs, experimental information is available[76–78] owing to the possible application of HEAs in magnetic refridgeration.[21]

B. Cluster expansion

The initial distribution of chemical species among the sites of a lattice determines the final relaxed configuration Γ and its relaxed energy $V(\Gamma)$. The initial distribution can be represented by stating the chemical species σ_i occupying the lattice position i, which can be considered as a vector of species, $\vec{\sigma}$. Under the assumption that the energy is determined primarily by short-range interactions, it is natural to seek a representation of the energy as a sum of interactions whose strength diminishes with increasing range. This sum, which may include single-atom and pair as well as many-body interactions, can be justified through a perturbative expansion of the total energy.[42–44] Each term depends on the atomic species and their relative positions through

$$V(\vec{\sigma}) = \sum_i E(\sigma_i) + \sum_{ij} J_{ij}(\sigma_i, \sigma_j)$$
$$+ \sum_{ijk} K_{ijk}(\sigma_i, \sigma_j, \sigma_k) + \cdots \quad .$$

$$(21)$$

The functions E, J, K, ... can be fit to a database of total energies for a variety of differently decorated

supercells of a basic lattice. The alloy theoretic automated toolkit (ATAT[79]) systematized a data generation and fitting procedure and provided tools to utilize the cluster expansion as an effective Hamiltonian for use in Monte Carlo simulation. By combining Monte Carlo with thermodynamic integration, ATAT allows the user to calculate free energies of many distinct phases, and thus to predict phase diagrams exhibiting order–disorder transitions and phase separation.[80] Later enhancements[81] include the possibility to incorporate vibrational and electronic free energy so that instead of expanding the relaxed total energy V, instead it can expand the basin free energy $F(\Gamma)$ [Eq. (19)].

In Fig. 3, we illustrate a cluster expansion for the binary refractory alloy system Mo–Ta. Elemental Mo and Ta both take the BCC structure, and many decorations of the BCC lattice with Mo and Ta atoms exhibit negative enthalpies of formation. The comparison of DFT energies with the best fit cluster expansion shows a typical fit, achieving a cross-validation error of 3 meV/atom with a set of 17 pair interactions J_{ij} and 13 triplets K_{ijl}. The convex hull contains 9 predicted ground states at a discrete set of compositions, separated by regions of phase coexistence. Ground state structures are labeled by their Pearson symbols. These ground states are not readily experimentally accessible because the dense set of structures lying close in energy above the convex hull allows for a large configurational entropy that stabilizes the experimentally observed continuous solid solution at elevated temperatures. Cluster expansions are a natural starting point for application of mean field theories to predict order–disorder of segregation phase transitions.[69,70]

C. First-principles hybrid Monte Carlo/molecular dynamics

Monte Carlo simulation is a popular method for generating structures representative of the equilibrium
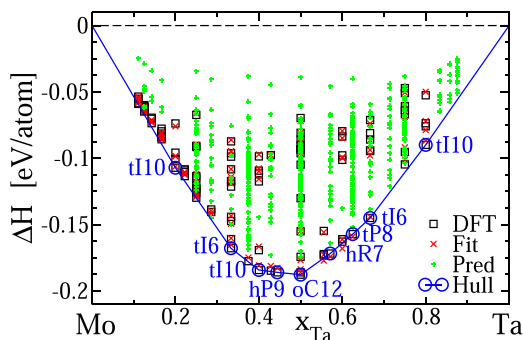

FIG. 3. Cluster expansion enthalpies for the BCC Mo–Ta binary alloy (see also Ref. 69). The data set of DFT-calculated enthalpies is shown with black squares and the fitted cluster expansion is shown with red crosses. Additional predicted structures with up to 9 atoms per cell are shown as green plus signs. Vertices of the convex hull (blue circles) identify stable structures labeled with their Pearson symbols. (color online)

ensemble. By attempting to swap the positions of different chemical species and weighting the acceptance probability of the swap by the Boltzmann factor $e^{-\Delta E/k_B T}$, suitable short- or long-ranged chemical order will develop. Molecular dynamics is an alternative method to explore configuration space. By integrating the equations of motion, it generates physically appropriate trajectories through the configuration space. Combining the two exploits the strengths of each to overcome inherent weaknesses of the other. While in principle molecular dynamics can access the full configuration space, in practice for solids, the atomic diffusion rates are too low to efficiently sample different chemical ordering in distinct basins Γ. This is where Monte Carlo excels. Meanwhile, Monte Carlo swaps of chemical species do not generate small atomic displacements typical of atomic vibrations within a given basin Γ. This is where molecular dynamics excels. This hybrid method proves highly efficient for simulation of HEAs.[82]

To further enhance equilibration, MC/MD can be supplemented with replica exchange,[83] in which independent runs at neighboring temperatures are swapped with a Boltzmann-like probability $e^{\Delta(1/T)\Delta E}$. In this manner, the proper weighting of the equilibrium ensemble is maintained at every temperature, while ensemble diversity is enhanced by swapping in independent configurations. An important variant of this method utilizes replicas with differing compositions and swaps atomic species between cells.[84]

Hybrid MC/MD has been extensively applied to refractory alloys.[4,65,75,85,86] Figure 4(a) shows the structure of $Al_{1.33}CoCrFeNi$ at $T = 300$ K simulated using hybrid MC/MD with replica exchange. The basic structure is BCC, but lattice distortion is evident in the displacement of atoms from their ideal positions. The lattice distortion arises from a combination of a static atomic size effect and a dynamic contribution from thermal atomic vibrations.[75,86] In terms of the mean square deviation from ideal sites $\langle|\Delta\mathbf{R}|^2\rangle$, the lattice distortion reduces the diffraction peak intensity at the reciprocal lattice vector $\mathbf{G}$ by the Debye–Waller factor e^{-2W} with $2W = \frac{1}{3}\langle|\Delta\mathbf{R}|^2\rangle|\mathbf{G}|^2$ and also creates diffuse scattering in the vicinity of the Bragg peaks.[75] Local atomic species-resolved lattice distortion can also be experimentally probed through XAFS.[87] Chemical ordering is evident in the alternation of Al-rich and transition metal-rich columns (see near the upper right-hand corner of the cell). The equilibrium phase at this composition contains domains of B2-like order and also tends to segregate Cr atoms from the other species[68] (see near the lower right-hand corner). This is perhaps clearer to visualize in the radial distribution functions shown in Fig. 4(b). First examine the distribution of atoms surrounding Al. The transition metal atoms, especially Co and Ni, primarily lie at the near-neighbor distance from
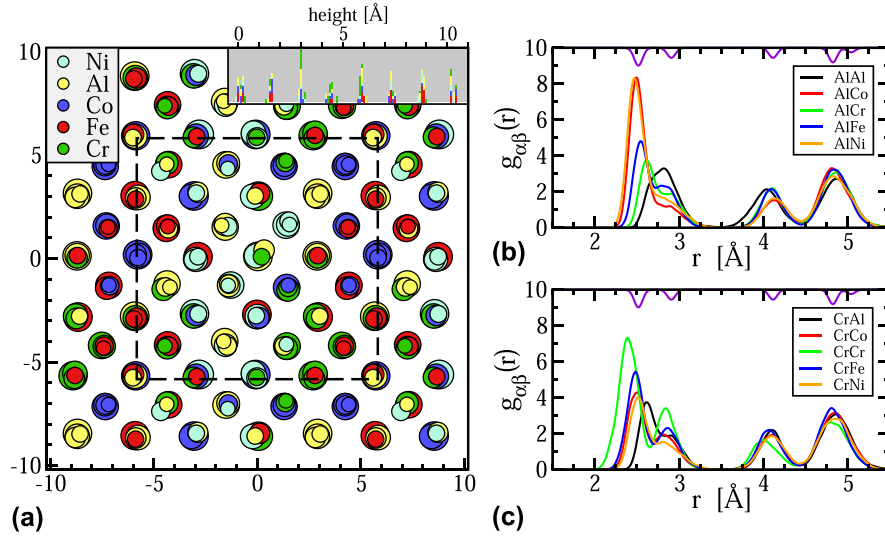
FIG. 4. (a) Simulated structure of $Al_{1.33}CoCrFeNi$ at $T = 300$ K viewed along the [001] direction. Colors indicate atomic species while sizes indicate vertical height. The simulation cell is outlined in dashed lines and extends periodically outside. The inset shows the vertical density profile. (b) and (c) Partial radial distribution functions $g_{\alpha\beta}(r)$ showing the atomic distributions around Al and Cr atoms. Purple curve at top is radial distribution function of elemental Cr. (color online)

Al, while the Al atoms lie at the second neighbor distance from each other. Meanwhile, notice the strong nearest and second neighbor peaks of Cr with itself.

D. Correlation functions and mutual information

Given a set of configurations selected from the equilibrium ensemble by Monte Carlo simulation of using either a cluster expansion or hybrid MC/MD, a variety of statistical and geometrical properties of the ensemble can be computed. Of particular interest are correlation functions,[88] notably the near neighbor pair frequencies $y_{\alpha\beta}$. The ratio between these frequencies and their uncorrelated expectations, e.g., $y_{\alpha\beta}/x_\alpha x_\beta$, reveals the preference for certain chemical species to associate. Figure 4 illustrates the nearest neighbor (NN) pair correlation functions from MC/MD replica exchange simulations of $Al_{1.33}CoCrFeNi$. Notice how the deviations of $y_{\alpha\beta}/x_\alpha x_\beta$ from 1 grow as the temperature drops, with increasing frequency of Co and Ni as neighbors of Al (and corresponding loss of these species as their own neighbors), and similarly the increasing frequency of Cr as its own neighbor.

Short-range chemical order necessarily reduces the configurational entropy relative to the ideal mixing value of Eq. (1). The correlation function $y_{\alpha\beta}$ provides information about the likely chemical species β occupying a site adjacent to any given atom of species α. This can be quantified through the notion of mutual information

$$I[y_{\alpha\beta}; \ x_\alpha] = \sum_{\alpha\beta} y_{\alpha\beta} \ln(y_{\alpha\beta}/x_\alpha x_\beta) \quad . \quad (22)$$

In view of the equivalence of entropy and information, the mutual information can be subtracted from the ideal
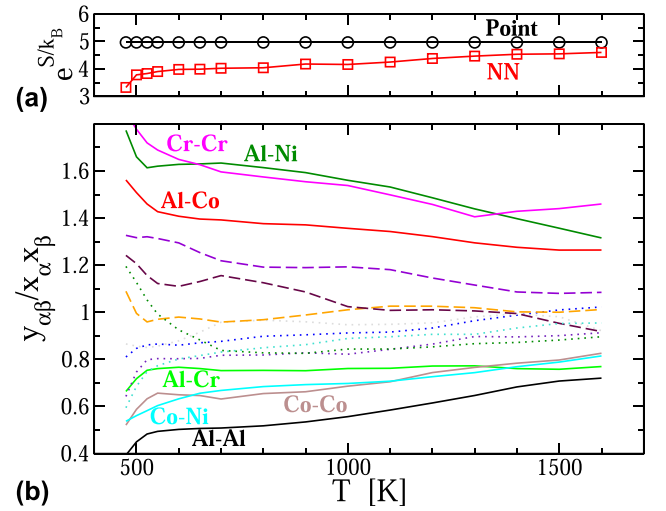

FIG. 5. Entropy and pair correlations $y_{\alpha\beta}/x_\alpha x_\beta$ of $Al_{1.33}CoCrFeNi$ obtained from MC/MD simulation with replica exchange. In (a), the single point (ideal mixing) entropy is reduced by the information content of the NN pair correlations [see Eq. (23)]. In (b), species pairs $\alpha\beta$ that deviate strongly from independence are labeled. (color online)

entropy to derive an improved estimate of the true entropy,[89,90]

$$S \approx S_{ideal} - 4k_B I[y_{\alpha\beta}; \ x_\alpha] \quad , \quad (23)$$

where the factor of 4 arises because there are 4 NN bonds per site. This expression can also be derived as a special case of Kikuchi's cluster variation method,[75,91,92] and it can be generalized to liquids.[90] Applying Eq. (1) to the composition $Al_{1.33}CoCrFeNi$ results in $S_{ideal} = 1.602k_B$ or $e^{S/k_B} = 4.96$. This value is shown in Fig. 5(a) and

J. Mater. Res., Vol. 0, No. 0, 2018

9

labeled as "Point" because each single site contributes independently. Notice that the value of S is slightly less than $\ln(5) = 1.609$ because the composition deviates slightly from equiatomic. The entropy loss due to the mutual information of "NN" pairs is small at high temperatures close to melting but grows substantially as temperature drops.

E. CALPHAD

CALPHAD is the last major technique we shall introduce. Standing for Calculation of Phase Diagrams, CALPHAD is based on interpolation techniques for thermodynamic functions, utilizing experimental or first-principles computed data for elements, and known binary and ternary alloy systems, to approximate the free energies of phases at compositions where data are lacking.[8] Interpolation on this data set yields approximate free energies $G^{(i)}(T; \mathbf{x}^{(i)})$ for multiple phases i at specified compositions or composition ranges. Finally, the convex hull is computed over a desired range of compositions and temperatures. Several companies offer databases and associated software tools, notably PANDAT and Thermo-Calc,[93] each of which have developed databases geared toward the study of HEAs. There is also an open source effort.[94]

The validity of CALPHAD rests on the accuracy and completeness of its underlying database. Traditional databases were structured around one or a few base elements such as aluminum, iron, or nickel, with additional alloying elements intended to be present in low concentrations. Thermodynamic data for intermetallic compounds at intermediate compositions are sparse, and existing phases are often absent from the databases, requiring careful adjustment and optimization when a new alloy system is to be explored. Nonetheless, CALPHAD is an invaluable tool for obtaining a qualitative global view of the phase diagram, including many of the potential phases that may occur and how phase selection is affected by variation of temperature and composition. It can motivate critical experiments that in turn can be used to revise and improve the database. Several example applications of CALPHAD to HEAs and MPEAs are given below.

V. EXAMPLE APPLICATIONS

Many pioneering studies in HEAs exemplify the above techniques and shed light on their structures and phase stability. In the following, a few examples of the application of CPA, supercells, cluster expansion, and finally CALPHAD are described.

A. CPA

We begin with example applications of the CPA. One of the first papers on HEA mentioned the BCC to FCC transition in $Al_y(CoCrFeNi)_{1-y}$ as the Al content y increases.[2,95] Note that this composition can also be written as $Al_xCrCoFeNi$, with $y = x/(4 + x)$. Figure 6 plots the CPA-calculated free energies[96] of the BCC phase (black) and the FCC phase (red) as functions of y. The enthalpies are taken from the CPA, while the entropies are assumed to be ideal mixing, i.e., Eq. (1) with $x_{Al} = y$ and $x_\alpha = (1 - y)/4$ for CoCrFeNi. The two curves cross near $y = 2$, indicating an exchange of stability, with greater Al content to the right favoring BCC and lower Al content to the left favoring FCC. However, the crossing region itself is thermodynamically unstable, as the pure phase free energies lie above the convex hull, defined by the common tangent construction and indicated in green. For Al content in this region from $y = 0.13$ to $y = 0.24$, a two phase mixture of FCC and BCC is predicted.

This prediction is in excellent agreement with experiments on the HEA $Al_y(CrCoFeNi)_{1-y}$,[95,97] which exhibit single phase FCC at low Al content and single phase BCC at high Al content, with mixed FCC and BCC in between. We can understand this progression qualitatively from the perspective of valance electron count (VEC). Scanning across the periodic table, we see that BCC structures are prevalent at low valence and FCC structures are prevalent at high valence. Moving to alloys (both simple binaries[98] and HEAs[4,99,100]), it appears that BCC extends up to VEC about 6.5 or 6.87, and FCC beyond 7.8 or 8, with complex structures, mixed behavior or phase coexistence expected in between.

CPA is also capable of modeling chemical ordering. The Strukturbericht L1$_2$ (Pearson cP4, prototype AuCu$_3$) structure singles out the cube corner site in the FCC unit cell relative to the three face center sites. A study by Niu et al.[101] addresses the chemical ordering of CrCoFeNi on the FCC lattice by preferentially occupying the cube corner site with one of the four species. They showed that separating the Cr atom significantly lowers the energy and that this energy drop is related to the antiferromagnetic spin orientation of Cr relative to the remaining
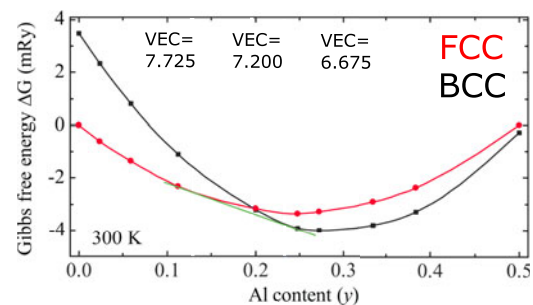

FIG. 6. Gibbs free energy $G = H - TS$ of $Al_y(CrCoFeNi)_{1-y}$ as a function of aluminum content y. Calculated at $T = 300$ K (adapted with permission from Ref. 96). VEC is the valence electron count. (color online)

elements. A more general CPA-based study of chemical ordering in $Al_xCrCoFeNi$ utilized calculated the linear response of the energy to general spatial variation in composition.[100] In the equiatomic compound $x = 1$, they predict depletion of Fe at the cube corner for FCC structures, and creation of Strukturbericht B2 (Pearson cP2, prototype CsCl) order between Al and Co at cube corner and body center, respectively, in the BCC phase. The magnetically driven phase transformation may mechanically strengthen the HEA.[102]

B. Supercell with first-principles entropies

Beyond the CPA, Feng et al.[65] calculated the free energy of a previously unknown quaternary, CrMoNbV, through explicit inclusion of configurational, vibrational, and electronic free energies (see Fig. 7). This quaternary was chosen because expected competition from precipitation of a CrNbV Laves phase made it an interesting test of the concept of entropic stabilization. Hybrid Monte Carlo/molecular dynamics simulations were used to generate supercells with suitable chemical short-ranged order, resulting in approximately 10% enhancements of near-neighbor frequencies of pairs from different columns of the periodic table (Cr and Mo each prefer to be neighbors of V and Nb). Chemical short-ranged order reduces enthalpies by approximately 6 meV/atom; however, the order is sufficiently weak that the loss of substitutional entropy as given by Eq. (23) is negligible. Competing phase free energies were likewise calculated, including Cr–V substitutional entropy on one of the sublattices of CrNbV as given by Eq. (20). By calculating

the free energy difference between the two phase mixture and the original equiatomic HEA, as a function of the CrNbV fraction precipitated, a transition was predicted at $T = 1600$ K. Subsequent experimental test confirmed a reversible transition from the two-phase mixture at low temperatures to the single-phase HEA at high temperatures. All terms in the entropy (configurational, vibrational, and electronic) favored the HEA, with the configurational term being dominant.

A similar approach[103] applied to the Mo–Nb–Ta–V–W quinary refractory HEA and its alloy subsystems calculated $G(x, T)$ for 178 potentially competing phases, from pure elements up through the HEA. It determined the full temperature-dependent phase diagrams of the quinary and the five constituent quaternary alloy systems.

C. Extrapolation from binaries

Recognizing that binary alloys are frequent and potent competitors for stability against HEAs, a group from Oak Ridge National Lab proposed to seek stable single phases by restricting the formation enthalpies of their constituent binary subsystems to a narrow range from modestly negative (compound-forming) to weakly positive (segregating).[104] Lower (i.e., most negative) enthalpy limits were set by the value of $-T_{Annealing}\Delta S_{Mixing}$, while upper limits were set by a similar requirement against phase separation. They took data from existing databases of first-principles formation enthalpy, several of which are available online (see Fig. 8).[105–108] In this manner, it proved possible to rationalize the successful single-phase compounds such as FeCoNi alloyed with Cr, Pd, or Mn,
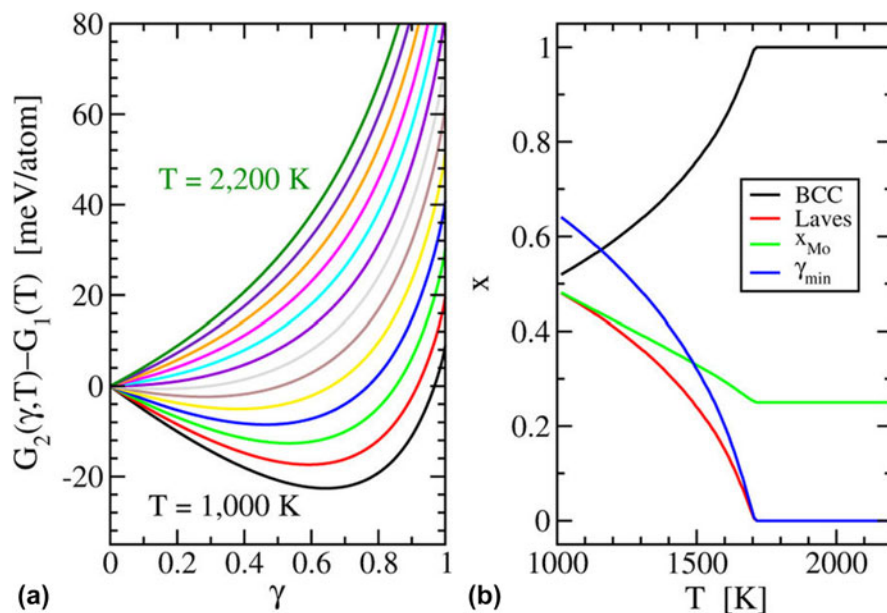

FIG. 7. (a) Free energy change from single phase HEA to a two-phase mixture; (b) Phase fractions as functions of temperature (reprinted with permission from Ref. 65; made available through the Creative Commons Attribution 4.0 International License [http://creativecommons.org/licenses/by/4.0/]). (color online)
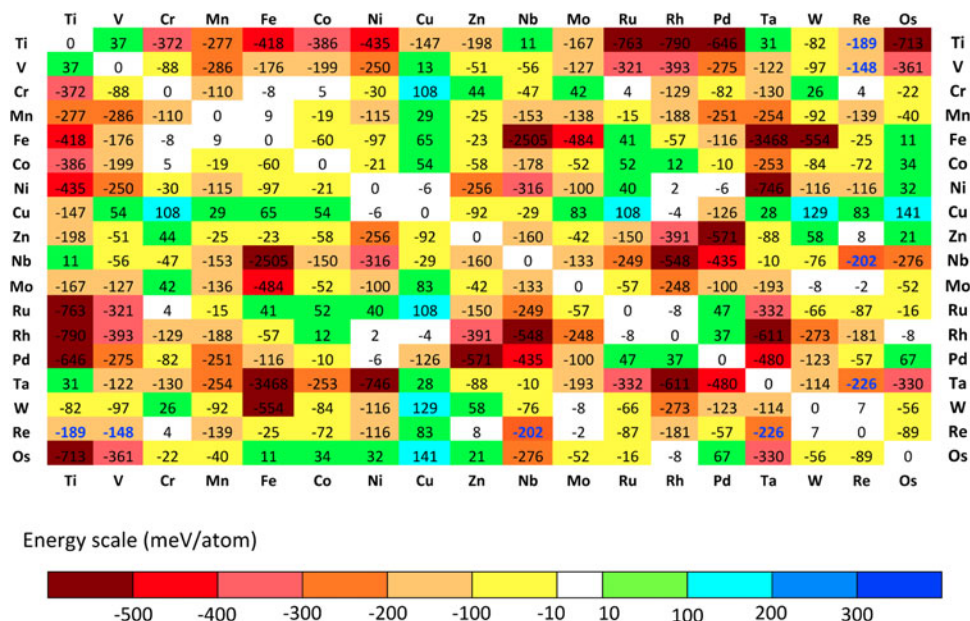
FIG. 8. Interaction energy matrix of Troparevsky et al. (reprinted with permission from Ref. 104; made available through the Creative Commons Attribution 3.0 License [https://creativecommons.org/licenses/by/3.0/]) based on data from AFLOW (Ref. 105) and the Alloy Database (Ref. 107). (color online)

but not with Mo, Ti, or V due to strong interactions with Fe and/or Ni.

The same approach implies a rapid fall-off of the number of potential single-phase compounds containing $N = 5$, 6, or 7 elements because each additional element is likely to interact unfavorably (either bind or repel too strongly) with one or more of the other elements in the compound. A generalization of this claim[6] suggests that in the composition space of an N-component alloy system, the stable compounds have an increasing probability to lie within M-component alloy subsystems, with $M < N$. The most likely values of M are 2 or 3. Thus, the use of binary interactions to screen for stability of multicomponent alloys is an excellent first approximation. If they were supplemented with data on ternaries then nearly all potential competitors would be accounted for.

D. Cluster expansions

Cluster expansions are effective Hamiltonians that efficiently describe the ground state energy of a given distribution of chemical constituents. They have been applied to several refractory element HEA-forming compounds based on BCC lattices, including the quinary Mo–Nb–Ta–V–W,[88] and three quaternaries, Cr–Mo–Nb–V,[65,75,85] Nb–Ti–V–Zr,[75,85] and Mo–Nb–Ta–W.[69,85,109] Given an effective Hamiltonian, rapid search can reveal ground states exhibiting a wide variety of differing patterns of chemical order in alloy ground states. They can also be utilized in Monte Carlo simulation to reveal
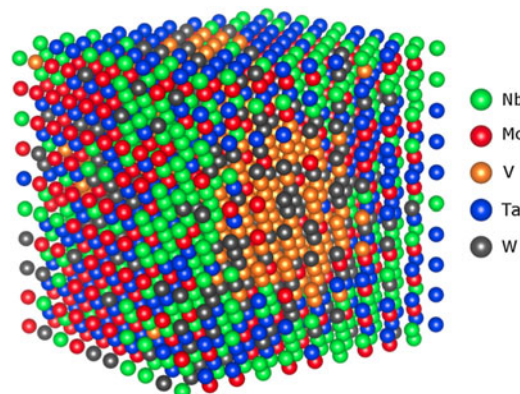

FIG. 9. Simulated structure of Mo–Nb–Ta–V–W at $T = 400$ K reveals domains of chemically ordered Mo–Ta, and partially segregated domains of Nb and V (reprinted with permission from Ref. 88). (color online)

temperature-driven order–disorder phase transitions. Figure 9 illustrates the outcome of such a simulation of Mo–Nb–Ta–V–W, which simultaneously displays domains of chemical order and phase separation along with partial substitutional disorder.[88] Specifically, Mo and Ta segregate into a domain that exhibits local B2-like chemical order, while Nb, and especially V, separate from each other and from Mo–Ta. Finally, W appears to mix readily into the other domains.

The prevalence of short-range order is illustrated in Fig. 10, which plots the diffuse diffraction intensities related to short-range chemical order in MoNbTaW. In
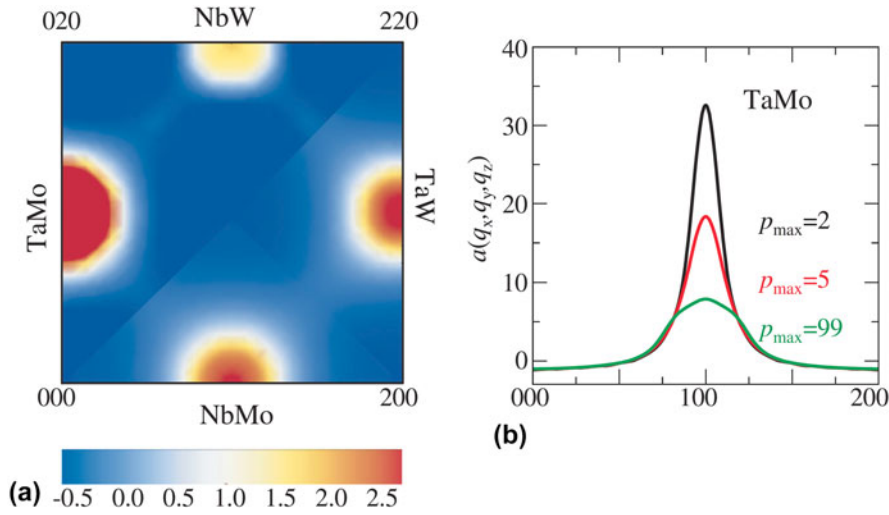
FIG. 10. (a) Diffuse diffraction peaks indicating short-ranged B2-type chemical order in simulations at $T = 1300$ K. (b) Including interactions of increasing range diminish the strength of the B2 short-range order (reprinted with permission from Ref. 109; made available through the Creative Commons Attribution License [http://creativecommons.org/licenses/by/4.0/]). (color online)

a BCC solid solution, Bragg peaks obey BCC extinction rules, namely the (hkl) peaks are extinct whenever $h + k + l$ is an odd integer. However, these odd peaks are present in chemically ordered variants of BCC such as B2. Short-ranged B2 order, like that seen between Mo and Ta in Fig. 9, can lead to diffuse peaks at the forbidden positions, as is shown in Fig. 10(a), which illustrates the intensity at positions $(hkl) = (010)$ for MoTa, (120) for NbW, (210) for TaW, and (100) for NbMo.

Fitting a cluster expansion is difficult. The series may require many terms,[109] even for a binary alloy, and the number of M-body terms grows roughly as N^M for N species. The number also grows rapidly with the diameter of the cluster. The series coefficients may converge poorly as additional terms are added. Regularization methods such as compressive sensing can significantly aid in fitting the coefficients of the cluster expansion,[110,111] but such tools have not been applied to HEAs to date. An illustration of the need for convergence is evident in Fig. 10(b), which shows that the strength of the Mo–Ta peak diminishes substantially as the number of pairwise interactions in the cluster expansion is increased.

Owing to small fitting errors in the cluster expansion, the cluster expansion ground states may not properly identify the true DFT ground states. It is profitable to carefully relax and converge the DFT energies of all the predicted ground states as well as the low-lying states above the convex hull. In this manner, it was possible to identify quaternary ground state structures[85] of MoNbTaW that were not identified by the original cluster expansion. These Pearson type hR7 ground state structures are illustrated in Fig. 11. Their crystal structures are given in Table I.
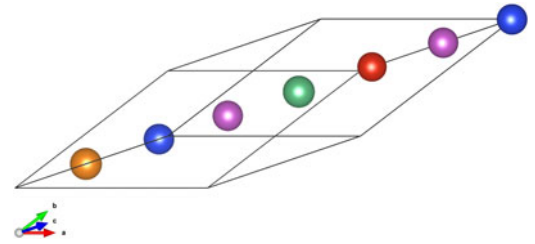

FIG. 11. Predicted (see Ref. 85) stable Pearson type hR7 quaternary phases $Mo_2NbTa_2W_2$ and $Mo_2Nb_2TaW_2$. Atomic species are colored as shown. The red position can be either Nb or Ta. (color online)

TABLE I. Crystallographic structure data of the predicted[85] stable quaternary phases $Mo_2NbTa_2W_2$ and $Mo_2Nb_2TaW_2$.

Pearson symbol hR7, space group $R3m$ (#160)			
Lattice parameters $a = 4.55$ Å, $c = 19.75$ Å, $\alpha = 90°$, $\gamma = 120°$			
Atom	Wyckoff	x	y	z
---	---	---	---	---
Ta1	**3a**	**0**	**0**	**0.142**
W1	3a	0	0	0.289
Mo1	3a	0	0	0.427
Nb1	3a	0	0	0.569
M = (Nb, Ta)	3a	0	0	0.716
Mo2	3a	0	0	0.859
W2	3a	0	0	0.997

E. CALPHAD method

CALPHAD has been widely applied to the study of HEAs and MPEAs because it provides fast screening of many alloy systems. A notable early effort to identify MPEAs with solid solution phases evaluated over 130,000 alloy systems.[5] In addition to a tentative classification of alloy systems into categories such as solid

solution-forming, intermetallic phase-forming, and mixed phase-forming, it provided a key conceptual advance. Contrary to the notion that increasing the number of components, N, necessarily favor formation of solid solutions through the increased configurational entropy, it turned out that the increased formation enthalpy of competing phases such as intermetallics grew more quickly than the $\ln(N)$ growth of the entropy. Hence, as N grows, the fraction of alloy systems exhibiting solid solution phases actually decreases, as illustrated in Fig. 12. The reason is that in the high dimensional composition space with large N, most extrema of the free energy occur on the surface of the space, corresponding to alloy subsystems containing fewer elements.[6]
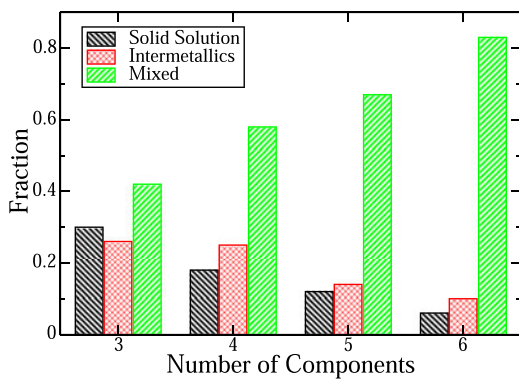

FIG. 12. Frequency of the structure as a function of the number of chemical species (adapted with permission from Ref. 5; made available through the Creative Commons Attribution 4.0 License [http://creativecommons.org/licenses/by/4.0/]). Solid solution denotes a single phase solid solution. Intermetallics denotes one or more complex intermetallic structures form. Mixed means at least one each of solid solution and intermetallic. (color online)
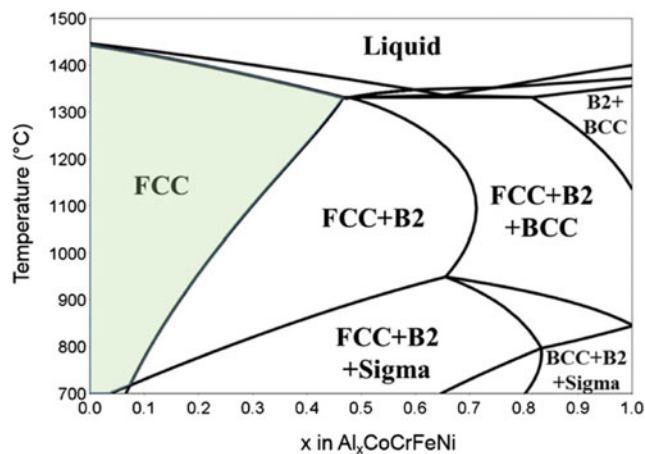

FIG. 13. CALPHAD-predicted phase diagram of Al$_x$CoCrFeNi (reprinted with permission from Ref. 112; made available through the Creative Commons Attribution 4.0 International License [http://creativecommons.org/licenses/by/4.0/]). Notice the shrinking range of the single-phase FCC solid solution as temperature drops.

An essential ingredient of the concept of HEAs is that the configurational entropy aids in stabilizing a single phase. Since the entropy enters the free energy multiplied by temperature, as TS, it is reasonable to expect that the HEA should be stable at high temperature but transform into an ordered structure or decompose into a mixture of ordered structures at low temperature. Indeed, the third law of thermodynamics, requiring that entropy vanishes in the limit as $T \rightarrow 0$ K, prevents solid–solid solutions in equilibrium at low temperature. Hence phase diagrams such as illustrated in Fig. 13[112] are typical of CALPHAD predictions for MPEAs. At high temperature, the FCC CoCrFeNi solid solution accepts Al to form Al$_x$CoCrFeNi up to $x = 0.4$. As temperature drops, the single-phase FCC region shrinks toward $x = 0$, losing stability first to a B2 phase consisting of chemical order between Al and transition metal atoms on a BCC lattice (see, e.g., Fig. 13), and then to a combination of B2 and a Cr-rich sigma phase.

VI. SUMMARY CONCLUSION

In summary, we reviewed basic principles of thermodynamics and the essential tools of quantum mechanics and statistical mechanics necessary to calculate thermodynamic stability from first principles. We gave several examples of their application to HEAs and related compounds. Specifically, we discussed the application of the CPA,[14,41,96,100,101,113–119] supercell and SQS methods,[38,40,66,120–123] empirical pair- and embedded atom-potentials,[124–131] and the Miedema approximation.[6,56,58–61,132–134] We explained how these may be combined for direct free energy calculation,[65,85,103,135] incorporated into cluster expansions,[69,70,85,88,109,136] used as the basis for computer simulation,[84–88,109,120,125,127,130,131,137,138] and exploited the resulting correlation functions.[4,75,85,90,92] Finally, we related these methods to the CALPHAD approach,[5,134,139–148] which historically has been empirical but now can be augmented with databases of first-principles derived information.

REFERENCES

1. B. Cantor, I.T.H. Chang, P. Knight, and A.J.B. Vincent: Microstructural development in equiatomic multicomponent alloys. *Mater. Sci. Eng., A* **375–377**, 213 (2004).
2. J-W. Yeh, S-K. Chen, S-J. Lin, J-Y. Gan, T-S. Chin, T-T. Shun, C-H. Tsau, and S-Y. Chang: Nanostructured high-entropy alloys with multiple principal elements: Novel alloy design concepts and outcomes. *Adv. Eng. Mater.* **6**, 299 (2004).
3. D.B. Miracle and O.N. Senkov: A critical review of high entropy alloys and related concepts. *Acta Mater.* **122**, 448 (2017).
4. M.C. Gao, C. Zhang, P. Gao, F. Zhang, L.Z. Ouyang, M. Widom, and J.A. Hawk: Thermodynamics of concentrated solid solution alloys. *Curr. Opin. Solid State Mater. Sci.* **21**, 238 (2017).
5. O.N. Senkov, J.D. Miller, D.B. Miracle, and C. Woodward: Accelerated exploration of multi-principal element alloys with solid solution phases. *Nat. Commun.* **6**, (2015).
6. M. Widom: Frequency estimate for multicomponent crystalline compounds. *J. Stat. Phys.* **167**, 726 (2017).
7. A. Zunger, S-H. Wei, L.G. Ferreira, and J.E. Bernard: Special quasirandom structures. *Phys. Rev. Lett.* **65**, 353 (1990).
8. H. Kaufman and L. Bernstein: *Computer Calculation of Phase Diagrams* (Academic Press, New York, 1970).
9. S. Murty, B.S. Yeh, and J-W. Ranganathan: *High-Entropy Alloys* (Butterworth-Heinemann, London, 2014).
10. M.C. Gao, J-W. Yeh, P.K. Liaw, and Y. Zhang: *High-Entropy Alloys* (Springer International Publishing, Cham, 2016).
11. D.B. Miracle: Critical assessment 14: High entropy alloys and their development as structural materials. *Mater. Sci. Technol.* **31**, 1142 (2015).
12. M-H. Tsai and J-W. Yeh: High-entropy alloys: A critical review. *Mater. Res. Lett.* **2**, 107 (2014).
13. Y.F. Ye, Q. Wang, J. Lu, C.T. Liu, and Y. Yang: High-entropy alloy: Challenges and prospects. *Mater. Today* **19**, 349 (2016).
14. F. Tian: A review of solid-solution models of high-entropy alloys based on ab initio calculations. *Front. Mater.* **4**, 36 (2017).
15. E.J. Pickering and N.G. Jones: High-entropy alloys: A critical assessment of their founding principles and future prospects. *Int. Mater. Rev.* **61**, 183 (2016).
16. Y. Ikeda, B. Grabowski, and F. Koermann: Ab initio phase stabilities and mechanical properties of multicomponent alloys: A comprehensive review for high entropy alloys and compositionally complex alloys. *Mater. Charact.* (2018). (to appear).
17. O.N. Senkov, G.B. Wilks, J.M. Scott, and D.B. Miracle: Mechanical properties of $Nb_{25}Mo_{25}Ta_{25}W_{25}$ and $V_{20}Nb_{20}Mo_{20}Ta_{20}W_{20}$ refractory high entropy alloys. *Intermetallics* **19**, 698 (2011).
18. O.N. Senkov, S.V. Senkova, D.B. Miracle, and C. Woodward: Mechanical properties of low-density, refractory multi-principal element alloys of the Cr–Nb–Ti–V–Zr system. *Mater. Sci. Eng., A* **565**, 51 (2013).
19. B. Gludovatz, A. Hohenwarter, D. Catoor, E.H. Chang, E.P. George, and R.O. Ritchie: A fracture-resistant high-entropy alloy for cryogenic applications. *Science* **345**, 1153 (2014).
20. Y. Zhang, G.M. Stocks, K. Jin, C. Lu, H. Bei, B.C. Sales, L. Wang, L.K. Béland, R.E. Stoller, G.D. Samolyuk, M. Caro, A. Caro, and W.J. Weber: Influence of chemical disorder on energy dissipation and defect evolution in concentrated solid solution alloys. *Nat. Commun.* **6**, 8736 (2015).
21. M. Kurniawan, A. Perrin, P. Xu, V. Keylin, and M. McHenry: Curie temperature engineering in high entropy alloys for magnetocaloric applications. *IEEE Magn. Lett.* **7**, 1 (2016).
22. D. Berardan, A.K. Meena, S. Franger, C. Herrero, and N. Dragoe: Controlled Jahn-Teller distortion in (MgCoNiCuZn)O-based high entropy oxides. *J. Alloys Compd.* **704**, 693 (2017).
23. D. Bérardan, S. Franger, A.K. Meena, and N. Dragoe: Room temperature lithium superionic conductivity in high entropy oxides. *J. Mater. Chem. A* **4**, 9536 (2016).
24. D. Bérardan, S. Franger, D. Dragoe, A.K. Meena, and N. Dragoe: Colossal dielectric constant in high entropy oxides. *Phys. Status Solidi RRL* **10**, 328 (2016).
25. P.B. Meisenheimer, T.J. Kratofil, and J.T. Heron: Giant enhancement of exchange coupling in entropy-stabilized oxide heterostructures. *Sci. Rep.* **7**, 13344 (2017).
26. S. Shafeie, S. Guo, Q. Hu, H. Fahlquist, P. Erhart, and A. Palmqvist: High-entropy alloys as high-temperature thermoelectric materials. *J. Appl. Phys.* **118**, 184905 (2015).
27. Z. Fan, H. Wang, Y. Wu, X.J. Liu, and Z.P. Lu: Thermoelectric high-entropy alloys with low lattice thermal conductivity. *RSC Adv.* **6**, 52164 (2016).
28. P. Hohenberg and W. Kohn: Inhomogeneous electron gas. *Phys. Rev.* **136**, B864 (1964).
29. W. Kohn and L.J. Sham: Self-consistent equations including exchange and correlation effects. *Phys. Rev.* **140**, A1133 (1965).
30. J.P. Perdew and A. Zunger: Self-interaction correction to density-functional approximations for many-electron systems. *Phys. Rev. B* **23**, 5048 (1981).
31. J.P. Perdew, K. Burke, and M. Ernzerhof: Generalized gradient approximation made simple. *Phys. Rev. Lett.* **77**, 3865 (1996).
32. P.E. Blöchl: Projector augmented-wave method. *Phys. Rev. B* **50**, 17953 (1994).
33. G. Kresse and D. Joubert: From ultrasoft pseudopotentials to the projector augmented-wave method. *Phys. Rev. B* **59**, 1758 (1999).
34. M. Mihalkovič and M. Widom: Ab initio calculations of cohesive energies of Fe-based glass-forming alloys. *Phys. Rev. B: Condens. Matter Mater. Phys.* **70**, 1 (2004).
35. M. Widom and M. Mihalkovic: Stability of Fe-based alloys with structure type C_6Cr_{23}. *J. Mater. Res.* **20**, 237 (2005).
36. G. Kresse and J. Hafner: Ab initio molecular dynamics for liquid metals. *Phys. Rev. B* **47**, 558 (1993).
37. W. Kohn: Density functional and density matrix method scaling linearly with the number of atoms. *Phys. Rev. Lett.* **76**, 3168 (1996).
38. M.C. Gao, C. Niu, C. Jiang, and D.L. Irving: *High-Entropy Alloy* (Springer International Publishing, Cham, 2016); pp. 333–368.
39. A. van de Walle, P. Tiwary, M. de Jong, D.L. Olmsted, M. Asta, A. Dick, D. Shin, Y. Wang, L-Q. Chen, and Z-K. Liu: Efficient stochastic generation of special quasirandom structures. *Calphad* **42**, 13 (2013).
40. C. Jiang and B.P. Uberuaga: Efficient ab initio modeling of random multicomponent alloys. *Phys. Rev. Lett.* **116**, 105501 (2016).
41. F. Yonezawa and K. Morigaki: Coherent potential approximation. *Prog. Theor. Phys. Suppl.* **53**, 1 (1973).
42. J.A. Moriarty: Density-functional formulation of the generalized pseudopotential theory. *Phys. Rev. B* **16**, 2537 (1977).
43. J.A. Moriarty: Analytic representation of multi-ion interatomic potentials in transition metals. *Phys. Rev. B* **42**, 1609 (1990).
44. J.A. Moriarty and M. Widom: First-principles interatomic potentials for transition-metal aluminides: Theory and trends across the 3d series. *Phys. Rev. B* **56**, 7905 (1997).
45. M. Mihalkovič and C.L. Henley: Empirical oscillating potentials for alloys from ab initio fits and the prediction of quasicrystal-

related structures in the Al–Cu–Sc system. *Phys. Rev. B* **85**, 092102 (2012).

46. M.S. Daw and M.I. Baskes: Embedded-atom method: Derivation and application to impurities, surfaces, and other defects in metals. *Phys. Rev. B* **29**, 6443 (1984).

47. S.M. Foiles, M.I. Baskes, and M.S. Daw: Embedded-atom-method functions for the fcc metals Cu, Ag, Au, Ni, Pd, Pt, and their alloys. *Phys. Rev. B* **33**, 7983 (1986).

48. M.W. Finnis and J.E. Sinclair: A simple empirical *N*-body potential for transition metals. *Philos. Mag. A* **50**, 45 (1984).

49. R.A. Johnson and D.J. Oh: Analytic embedded atom method model for bcc metals. *J. Mater. Res.* **4**, 1195 (1989).

50. F. Ercolessi and J.B. Adams: Interatomic potentials from first-principles calculations: The force-matching method. *Europhys. Lett.* **26**, 583 (1994).

51. M.I. Mendelev, S. Han, D.J. Srolovitz, G.J. Ackland, D.Y. Sun, and M. Asta: Development of new interatomic potentials appropriate for crystalline and liquid iron. *Philos. Mag.* **83**, 3977 (2003).

52. A.R. Miedema, P.F. de Châtel, and F.R. de Boer: Cohesion in alloys—Fundamentals of a semi-empirical model. *Phys. B* **100**, 1 (1980).

53. A.R. Miedema and A.K. Niessen: The enthalpy of solution for solid binary alloys of two 4*d*-transition metals. *Calphad* **7**, 27 (1983).

54. A.P. Gonçalves and M. Almeida: Extended Miedema model: Predicting the formation enthalpies of intermetallic phases with more than two elements. *Phys. B* **228**, 289 (1996).

55. M.S. Mousavi, R. Abbasi, and S.F. Kashani-Bozorg: A thermodynamic approach to predict formation enthalpies of ternary systems based on Miedema's model. *Metall. Mater. Trans. A* **47**, 3761 (2016).

56. A. Takeuchi and A. Inoue: Mixing enthalpy of liquid phase calculated by Miedema's scheme and approximated with sub-regular solution model for assessing forming ability of amorphous and glassy alloys. *Intermetallics* **18**, 1779 (2010).

57. A. Takeuchi, K. Amiya, T. Wada, K. Yubuta, W. Zhang, and A. Makino: Entropies in alloy design for high-entropy and bulk glassy alloys. *Entropy* **15**, 3810 (2013).

58. A. Takeuchi, M.C. Gao, J. Qiao, and M. Widom: *High-Entropy Alloys* (2016); p. 445. **[AU8]**

59. M.C. Gao, C.S. Carney, Ö.N. Doğan, P.D. Jablonksi, J.A. Hawk, and D.E. Alman: Design of refractory high-entropy alloys. *JOM* **67**, 2653 (2015).

60. Y. Zhang, Y.J. Zhou, J.P. Lin, G.L. Chen, and P.K. Liaw: Solid-solution phase formation rules for multi-component alloys. *Adv. Eng. Mater.* **10**, 534 (2008).

61. X. Yang and Y. Zhang: Prediction of high-entropy stabilized solid-solution in multi-component alloys. *Mater. Chem. Phys.* **132**, 233 (2012).

62. G.S. Pomrehn, E.S. Toberer, G.J. Snyder, and A. van de Walle: Entropic stabilization and retrograde solubility in Zn_4Sb_3. *Phys. Rev. B* **83**, 094106 (2011).

63. H. Zhang, S. Yao, and M. Widom: Predicted phase diagram of boron–carbon–nitrogen. *Phys. Rev. B* **93**, 144107 (2016).

64. M. Widom and W.P. Huhn: Prediction of orientational phase transition in boron carbide. *Solid State Sci.* **14**, 1648 (2012).

65. R. Feng, P.K. Liaw, M.C. Gao, and M. Widom: First-principles prediction of high-entropy-alloy stability. *npj Comput. Mater.* **3**, 50 (2017).

66. L. Rogal, P. Bobrowski, F. Körmann, S. Divinski, F. Stein, and B. Grabowski: Computationally-driven engineering of sublattice ordering in a hexagonal AlHfScTiZr high entropy alloy. *Sci. Rep.* **7**, 2209 (2017).

67. Y. Qiu, Y.J. Hu, A. Taylor, M.J. Styles, R.K.W. Marceau, A.V. Ceguerra, M.A. Gibson, Z.K. Liu, H.L. Fraser, and

N. Birbilis: A lightweight single-phase AlTiVCr compositionally complex alloy. *Acta Mater.* **123**, 115 (2017).

68. L.J. Santodonato, Y. Zhang, M. Feygenson, C.M. Parish, M.C. Gao, R.J.K. Weber, J.C. Neuefeind, Z. Tang, and P.K. Liaw: Deviation from high-entropy configurations in the atomic distributions of a multi-principal-element alloy. *Nat. Commun.* **6**, 5964 (2015).

69. W.P. Huhn and M. Widom: Prediction of A2 to B2 phase transition in the high-entropy alloy Mo–Nb–Ta–W. *JOM* **65**, 1772 (2013).

70. Y. Lederer, C. Toher, K.S. Vecchio, and S. Curtarolo: The search for high entropy alloys: A high-throughput ab initio approach (2017). https://arxiv.org/abs/1711.03426.

71. W.L. Bragg and E.J. Williams: The effect of thermal agitation on atomic arrangement in alloys. *Proc. R. Soc. London, Ser. A* **145**, 699 (1934).

72. R.H. Fowler and E.A. Guggenheim: Statistical thermodynamics of super-latices. *Proc. R. Soc. London, Ser. A* **174**, 189 (1939).

73. H.A. Bethe: Statistical theory of superlattices. *Proc. R. Soc. London, Ser. A* **150**, 552 (1935).

74. R. Kikuchi: A theory of cooperative phenomena. *Phys. Rev.* **81**, 988 (1951).

75. M. Widom: Entropy and diffuse scattering: Comparison of NbTiVZr and CrMoNbV. *Metall. Mater. Trans. A* **47**, 3306 (2016).

76. M.S. Lucas, D. Belyea, C. Bauer, N. Bryant, E. Michel, Z. Turgut, S.O. Leontsev, J. Horwath, S.L. Semiatin, M.E. McHenry, and C.W. Miller: Thermomagnetic analysis of $FeCoCr_xNi$ alloys: Magnetic entropy of high-entropy alloys. *J. Appl. Phys.* **113**, 17A923 (2013).

77. P. Li, A. Wang, and C.T. Liu: A ductile high entropy alloy with attractive magnetic properties. *J. Alloys Compd.* **694**, 55 (2017).

78. O. Schneeweiss, M. Friák, M. Dudová, D. Holec, M. Šob, D. Kriegner, V. Holý, P. Beran, E.P. George, J. Neugebauer, and A. Dlouhý: Magnetic properties of the CrMnFeCoNi high-entropy alloy. *Phys. Rev. B* **96**, 014437 (2017).

79. A. Van de Walle, M. Asta, and G. Ceder: The alloy theoretic automated toolkit: A user guide. *CALPHAD: Comput. Coupling Phase Diagrams Thermochem.* **26**, 539 (2002).

80. C. Ravi, B.K. Panigrahi, M.C. Valsakumar, and A. van de Walle: First-principles calculation of phase equilibrium of V–Nb, V–Ta, and Nb–Ta alloys. *Phys. Rev. B* **85**, 054202 (2012).

81. A. van de Walle: Multicomponent multisublattice alloys, non-configurational entropy and other additions to the alloy theoretic automated toolkit. *CALPHAD: Comput. Coupling Phase Diagrams Thermochem.* **33**, 266 (2009).

82. M. Widom, W.P. Huhn, S. Maiti, and W. Steurer: Hybrid Monte Carlo/molecular dynamics simulation of a refractory metal high entropy alloy. *Metall. Mater. Trans. A* **45**, 196 (2014).

83. S. Yao, Q. Gao, and M. Widom: Phase diagram of boron carbide with variable carbon composition. *Phys. Rev. B* **95** (2017).

84. C. Niu, W. Windl, and M. Ghazisaeidi: Multi-cell Monte Carlo relaxation method for predicting phase stability of alloys. *Scr. Mater.* **132**, 9 (2017).

85. M. Widom: In *High-Entropy Alloys: Fundamentals and Applications*, Y. Gao, M.C. Yeh, J-W. Liaw, and P.K. Zhang, eds. (Springer International Publishing, Cham, 2016); pp. 267–298. **[AU9]**

86. B. Feng and M. Widom: Elastic stability and lattice distortion of refractory high entropy alloys. *Mater. Chem. Phys.* **210**, 309 (2018).

87. H. Oh, D. Ma, G. Leyson, B. Grabowski, E. Park, F. Körmann, and D. Raabe: Lattice distortions in the FeCoNiCrMn high entropy alloy studied by theory and experiment. *Entropy* **18**, 321 (2016).

88. A. Fernández-Caballero, J.S. Wróbel, P.M. Mummery, and D. Nguyen-Manh: Short-range order in high entropy alloys:

16

J. Mater. Res., Vol. 0, No. 0, 2018

Theoretical formulation and application to Mo–Nb–Ta–V–W system. *J. Phase Equilib. Diffus.* **38**, 391 (2017).

89. E.T. Jaynes: Information theory and statistical mechanics. *Phys. Rev.* **106**, 620 (1957).

90. M.C. Gao and M. Widom: Information entropy of liquid metals. *J. Phys. Chem. B* **122**, 3550 (2018).

91. R. Kikuchi: Second Hessian determinant as the criterion for order (first or second) of phase transition. *Phys. A* **142**, 321 (1987).

92. M.C. Gao, P. Gao, J.A. Hawk, L. Ouyang, D.E. Alman, and M. Widom: Computational modeling of high-entropy alloys: Structures, thermodynamics and elasticity. *J. Mater. Res.* **32**, 3627 (2017).

93. H. Mao, H-L. Chen, and Q. Chen: TCHEA1: A thermodynamic database not limited for "high entropy" alloys. *J. Phase Equilib. Diffus.* **38**, 353 (2017).

94. Open CALPHAD: http://www.opencalphad.com/ (n.d.).

95. W-R. Wang, W-L. Wang, S-C. Wang, Y-C. Tsai, C-H. Lai, and J-W. Yeh: Effects of Al addition on the microstructure and mechanical property of Al$_x$CoCrFeNi high-entropy alloys. *Intermetallics* **26**, 44 (2012).

96. F. Tian, L. Delczeg, N. Chen, L.K. Varga, J. Shen, and L. Vitos: Structural stability of NiCoFeCrAl$_x$ high-entropy alloy from ab initio theory. *Phys. Rev. B* **88**, 085128 (2013).

97. Y-F. Kao, T-J. Chen, S-K. Chen, and J-W. Yeh: Microstructure and mechanical property of as-cast, -homogenized, and -deformed Al$_x$CoCrFeNi ($0 \leq x \leq 2$) high-entropy alloys. *J. Alloys Compd.* **488**, 57 (2009).

98. S. Lee and R. Hoffmann: Bcc and fcc transition metals and alloys: A central role for the Jahn-Teller effect in explaining their ideal and distorted structures. *J. Am. Chem. Soc.* **124**, 4811 (2002).

99. S. Guo, C. Ng, J. Lu, and C.T. Liu: Effect of valence electron concentration on stability of fcc or bcc phase in high entropy alloys. *J. Appl. Phys.* **109**, 103505 (2011).

100. P. Singh, A.V. Smirnov, and D.D. Johnson: Atomic short-range order and incipient long-range order in high-entropy alloys. *Phys. Rev. B: Condens. Matter Mater. Phys.* **91**, 1 (2015).

101. C. Niu, A.J. Zaddach, A.A. Oni, X. Sang, J.W. Hurt, J.M. LeBeau, C.C. Koch, and D.L. Irving: Spin-driven ordering of Cr in the equiatomic high entropy alloy NiFeCrCo. *Appl. Phys. Lett.* **106**, 161906 (2015).

102. C. Niu, C.R. LaRosa, J. Miao, M.J. Mills, and M. Ghazisaeidi: Magnetically-driven phase transformation strengthening in high entropy alloys. *Nat. Commun.* **9**, 1363 (2018).

103. Y. Wang, M. Yan, Q. Zhu, W.Y. Wang, Y. Wu, X. Hui, R. Otis, S-L. Shang, Z-K. Liu, and L-Q. Chen: Computation of entropies and phase equilibria in refractory V–Nb–Mo–Ta–W high-entropy alloys. *Acta Mater.* **143**, 88 (2018).

104. M.C. Troparevsky, J.R. Morris, P.R.C. Kent, A.R. Lupini, and G.M. Stocks: Criteria for predicting the formation of single-phase high-entropy alloys. *Phys. Rev. X* **5**, 1 (2015).

105. Automatic FLOW for Materials Discovery: http://aflowlib.org (2018).

106. The Materials Project: http://materialsproject.org (2018).

107. M. Widom and M. Mihalkovic: Alloy database: http://alloy.phys.cmu.edu (2018).

108. The Open Quantum Materials Database: http://oqmd.org (2018).

109. F. Körmann, A.V. Ruban, and M.H.F. Sluiter: Long-ranged interactions in bcc NbMoTaW high-entropy alloys. *Mater. Res. Lett.* **5**, 35 (2017).

110. L.J. Nelson, G.L.W. Hart, F. Zhou, and V. Ozoliņš: Compressive sensing as a paradigm for building physics models. *Phys. Rev. B: Condens. Matter Mater. Phys.* **87**, 1 (2013).

111. L.J. Nelson, V. Ozoliņš, C.S. Reese, F. Zhou, and G.L.W. Hart: Cluster expansion made easy with Bayesian compressive sensing. *Phys. Rev. B: Condens. Matter Mater. Phys.* **88**, 1 (2013).

112. C.D. Taylor, P. Lu, J. Saal, G.S. Frankel, and J.R. Scully: Integrated computational materials engineering of corrosion resistant alloys. *npj Mater. Degrad.* **2**, 6 (2018).

113. K.M. Youssef, A.J. Zaddach, C. Niu, D.L. Irving, and C.C. Koch: A novel low-density, high-hardness, high-entropy alloy with close-packed single-phase nanocrystalline structures. *Mater. Res. Lett.* **3**, 95 (2015).

114. C. Niu, A.J. Zaddach, C.C. Koch, and D.L. Irving: First principles exploration of near-equiatomic NiFeCrCo high entropy alloys. *J. Alloys Compd.* **672**, 510 (2016).

115. P. Cao, X. Ni, F. Tian, L.K. Varga, and L. Vitos: Ab initio study of Al$_x$MoNbTiV high-entropy alloys. *J. Phys.: Condens. Matter* **27**, 075401 (2015).

116. L-Y. Tian, Q-M. Hu, R. Yang, J. Zhao, B. Johansson, and L. Vitos: Elastic constants of random solid solutions by SQS and CPA approaches: The case of fcc Ti–Al. *J. Phys.: Condens. Matter* **27**, 315702 (2015).

117. F. Tian, Y. Wang, D.L. Irving, and L. Vitos: *High-Entropy Alloy* (Springer International Publishing, Cham, 2016); pp. 299–332.

118. F. Tian, L.K. Varga, N. Chen, L. Delczeg, and L. Vitos: Ab initio investigation of high-entropy alloys of 3d elements. *Phys. Rev. B* **87**, 075144 (2013).

119. F. Tian, L.K. Varga, J. Shen, and L. Vitos: Calculating elastic constants in high-entropy alloys using the coherent potential approximation: Current issues and errors. *Comput. Mater. Sci.* **111**, 350 (2016).

120. F. Körmann and M. Sluiter: Interplay between lattice distortions, vibrations and phase stability in NbMoTaW high entropy alloys. *Entropy* **18**, 403 (2016).

121. F. Körmann, Y. Ikeda, B. Grabowski, and M.H.F. Sluiter: Phonon broadening in high entropy alloys. *npj Comput. Mater.* **3**, 36 (2017).

122. Z. Leong, J.S. Wróbel, S.L. Dudarev, R. Goodall, I. Todd, and D. Nguyen-Manh: The effect of electronic structure on the phases present in high entropy alloys. *Sci. Rep.* **7**, 39803 (2017).

123. Z. Rak, C.M. Rost, M. Lim, P. Sarker, C. Toher, S. Curtarolo, J-P. Maria, and D.W. Brenner: Charge compensation and electrostatic transferability in three entropy-stabilized oxides: Results from density functional theory calculations. *J. Appl. Phys.* **120**, 095105 (2016).

124. S. Maiti and W. Steurer: Structural-disorder and its effect on mechanical properties in single-phase TaNbHfZr high-entropy alloy. *Acta Mater.* **106**, 87 (2016).

125. M. Meraj and S. Pal: Deformation of Ni$_{20}$W$_{20}$Cu$_{20}$Fe$_{20}$Mo$_{20}$ high entropy alloy for tensile followed by compressive and compressive followed by tensile loading: A molecular dynamics simulation based study. *IOP Conf. Ser.: Mater. Sci. Eng.* **115**, 012019 (2016).

126. J. Li, Q. Fang, B. Liu, Y. Liu, and Y. Liu: Mechanical behaviors of AlCrFeCuNi high-entropy alloys under uniaxial tension via molecular dynamics simulation. *RSC Adv.* **6**, 76409 (2016).

127. L. Xie, P. Brault, A-L. Thomann, X. Yang, Y. Zhang, and G. Shang: Molecular dynamics simulation of Al–Co–Cr–Cu–Fe–Ni high entropy alloy thin film growth. *Intermetallics* **68**, 78 (2016).

128. Z. Liu, Y. Lei, C. Gray, and G. Wang: Examination of solid-solution phase formation rules for high entropy alloys from atomistic Monte Carlo simulations. *JOM* **67**, 2364 (2015).

129. C. Varvenne, A. Luque, and W.A. Curtin: Theory of strengthening in fcc high entropy alloys. *Acta Mater.* **118**, 164 (2016).

130. W-M. Choi, Y.H. Jo, S.S. Sohn, S. Lee, and B-J. Lee: Understanding the physical metallurgy of the CoCrFeMnNi high-entropy alloy: An atomistic simulation study. *npj Comput. Mater.* **4**, 1 (2018).

131. W-M. Choi, Y. Kim, D. Seol, and B-J. Lee: Modified embedded-atom method interatomic potentials for the Co–Cr, Co–Fe,

J. Mater. Res., Vol. 0, No. 0, 2018

17

Co–Mn, Cr–Mn, and Mn–Ni binary systems. *Comput. Mater. Sci.* **130**, 121 (2017).

132. T.P. Yadav, S. Mukhopadhyay, S.S. Mishra, N.K. Mukhopadhyay, and O.N. Srivastava: Synthesis of a single phase of high-entropy Laves intermetallics in the Ti–Zr–V–Cr–Ni equiatomic alloy. *Philos. Mag. Lett.* **97**, 494 (2017).

133. M.G. Poletti, G. Fiore, B.A. Szost, and L. Battezzati: Search for high entropy alloys in the X–NbTaTiZr systems (X = Al, Cr, V, Sn). *J. Alloys Compd.* **620**, 283 (2015).

134. D.J.M. King, S.C. Middleburgh, A.G. McGregor, and M.B. Cortie: Predicting the formation and stability of single phase high-entropy alloys. *Acta Mater.* **104**, 172 (2016).

135. J.F. Fernandez, M. Widom, F. Cuevas, J.R. Ares, J. Bodega, F. Leardini, M. Mihalkovič, and C. Sánchez: First-principles phase stability calculations and estimation of finite temperature effects on pseudo-binary $Mg_6(Pd_xNi_{1-x})$ compounds. *Intermetallics* **19**, 502 (2010).

136. M.C. Gao, Y. Suzuki, H. Schweiger, Ö.N. Doğan, J. Hawk, and M. Widom: Phase stability and elastic properties of Cr–V alloys. *J. Phys.: Condens. Matter* **25** (2013).

137. Z. Wang, J. Li, Q. Fang, B. Liu, and L. Zhang: Investigation into nanoscratching mechanical response of AlCrCuFeNi high-entropy alloys using atomic simulations. *Appl. Surf. Sci.* **416**, 470 (2017).

138. A. Sharma, P. Singh, D.D. Johnson, P.K. Liaw, and G. Balasubramanian: Atomistic clustering-ordering and high-strain deformation of an $Al_{0.1}CrCoFeNi$ high-entropy alloy. *Sci. Rep.* **6**, 31028 (2016).

139. F. Zhang, C. Zhang, S.L. Chen, J. Zhu, W.S. Cao, and U.R. Kattner: An understanding of high entropy alloys from phase diagram calculations. *Calphad* **45**, 1 (2014).

140. K. Guruvidyathri, K.C. Hari Kumar, J.W. Yeh, and B.S. Murty: Topologically close-packed phase formation in high entropy alloys: A review of calphad and experimental results. *JOM* **69**, 2113 (2017).

141. C. Zhang, F. Zhang, S. Chen, and W. Cao: Computational thermodynamics aided high-entropy alloy design. *JOM* **64**, 839 (2012).

142. M. Gao and D. Alman: Searching for next single-phase high-entropy alloy compositions. *Entropy* **15**, 4504 (2013).

143. C. Zhang and M.C. Gao: *High-Entropy Alloy* (Springer International Publishing, Cham, 2016); pp. 399–444.

144. A. Durga, K.C. Hari Kumar, and B.S. Murty: Phase formation in equiatomic high entropy alloys: CALPHAD approach and experimental studies. *Trans. Indian Inst. Met.* **65**, 375 (2012).

145. J.E. Saal, I.S. Berglund, J.T. Sebastian, P.K. Liaw, and G.B. Olson: Equilibrium high entropy alloy phase stability from experiments and thermodynamic modeling. *Scr. Mater.* **146**, 5 (2018).

146. B. Zhang, M.C. Gao, Y. Zhang, and S.M. Guo: Senary refractory high-entropy alloy $Cr_xMoNbTaVW$. *Calphad* **51**, 193 (2015).

147. D. Ma, M. Yao, K.G. Pradeep, C.C. Tasan, H. Springer, and D. Raabe: Phase stability of non-equiatomic CoCrFeMnNi high entropy alloys. *Acta Mater.* **98**, 288 (2015).

148. W-M. Choi, S. Jung, Y.H. Jo, S. Lee, and B-J. Lee: Design of new face-centered cubic high entropy alloys by thermodynamic calculation. *Met. Mater. Int.* **23**, 839 (2017).

AUTHOR QUERY – jmr.2018.222

1. Please check whether the edits made to the sentence "It is also. . ." are correct.
2. In the sentence beginning "Section III addressed methods. . .," please confirm that "preceding section" refers to Section III.
3. Please check the sentence "Here r and p. . ." for clarity.
4. Please check the sentence "Mixed means at. . ." for clarity.
5. Details given in references '4 & 100' and '40 & 125' were same. Hence, references '100 and 125' have been deleted and the references have been renumbered accordingly.
6. Please provide the page range for reference '5'.
7. Please update references '16, 70, and 94'.
8. Please provide the publisher name and location for reference '58'.
9. Please provide the chapter title for reference '85'.

EDITOR QUERY – jmr.2018.222

There are no editor queries for this article.